Nonequilibrium molecular dynamics simulation of electro-osmotic flow in a charged nanopore

Aidan P. Thompson[a)]
Sandia National Laboratories, Albuquerque, New Mexico 87185

(Received 6 May 2003; accepted 22 July 2003)

Nonequilibrium molecular dynamics simulations were performed for Poiseuille and electro-osmotic flow in a charged cylindrical nanopore. The goal was to examine any deviations from continuum flow behavior and to compare and contrast the Poiseuille and electro-osmotic flow situations. The fluid was composed of cationic counterions and nonpolar monatomic solvent molecules. The cylindrical surface of the pore wall was represented by a stochastic scattering boundary condition. The lack of any surface roughness and the computational efficiency of the fluid model enabled the velocity profile near the wall to be measured at very high spatial resolution. The simulation results indicate that both Poiseuille and electro-osmotic flow conform to continuum transport theories except in the first monolayer of fluid at the pore wall. The apparent viscosity in this region was highly nonuniform and exhibited singularities. Despite this, the viscosity profiles obtained from Poiseuille and electro-osmotic flow were in good mutual agreement at all locations. The singularities were caused by a local maximum in the solvent and counterion velocity profiles occurring at the edge of the first monolayer of liquid. This apparent channeling of fluid near the pore wall has been observed in previous studies of Poiseuille flow. The exact cause is not clear, but it may be due to cooperative transport of the fluid molecules facilitated by two-dimensional ordering at the wall.
 [DOI: 10.1063/1.1609194]

I. INTRODUCTION

Electro-osmotic flow refers to motion of an electrolyte solution along a charged surface in response to an electric field. This phenomenon has been known since the early days of surface science. However, it has only recently become of practical interest, due to its usefulness as a method of transporting and also separating ionic solutions in microporous materials and microfluidic devices.

The currently accepted continuum theory of electro-osmotic flow was developed over a century ago by Smoluchowski and Helmholtz and is based on the concept of the diffuse electric double layer.[1] The introduction of an insulating solid surface into a polar liquid generally causes charge separation or the formation of an electric double layer. An immobile charge builds up in the solid at its surface, and an equal and opposite charge accumulates in a layer of fluid adjacent to the surface. This charged fluid layer may be structured, consisting of a thin immobile layer that is tightly bound to the solid surface and a diffuse mobile layer. It is the response of the charged mobile layer to the electric field that causes electro-osmotic flow. The fluid velocity at the wall is assumed to be zero, and rises monotonically to the maximum value at the outer edge of the diffuse layer. Beyond this point the velocity profile is uniform.

In the case of small pores where the diffuse layer extends over the entire pore cross section, the maximum flow velocity is reduced due to double layer overlap. Continuum models for this effect were developed by Rice and Whitehead,[2] Gross and Osterle,[3] and most recently by Pintauro and co-workers.[4] These models combine Navier–Stokes, Poisson–Boltzmann, and Nernst–Planck equations for fluid flow, double layer structure, and counterion transport, respectively. A fundamental difficulty with continuum models is that they can not represent the atomistic ordering of the fluid structure near the solid surface. In the case of pressure-driven flow in pores, atomistic phenomena have a negligible effect on the overall flowrate. This is because in all but the smallest pores most of the driving force for flow is applied to fluid which is sufficiently far from the wall that it behaves as a viscous continuum. However, in the case of electro-osmotic flow, the driving force for flow is strongest very close to the wall and this is also where atomistic effects are important. For example, the way in which the charge in the fluids partitions between the mobile and immobile layers strongly affects the overall flow rate. Because the effect of atomistic ordering could potentially be large for electro-osmotic flow in nanopores, rendering the continuum models inadequate, it is useful to test these models by direct comparison with simulations that include atomistic detail.

Methods for treating flow of simple fluids past uncharged solid surfaces using nonequilibrium molecular dynamics (NEMD) are now well established.[5–9] Most of these studies have considered either Couette or Poiseuille flow. The general conclusion has been that departures from ideal continuum behavior occur only within several molecular diameters from the solid surface. Beyond that, the observed fluid flow closely matches that predicted by the Navier–Stokes equation for Newtonian fluids.

More recently, there have been several equilibrium and nonequilibrium studies of electro-osmotic flow.[10–15] Most of

[a)]Electronic mail: athomps@sandia.gov

these studies used relatively detailed models of the pore wall and fluid. The computational cost of these models tended to limit the duration of the simulations. In the nonequilibrium studies, the relatively short simulation times limited the spatial resolution at which the velocity profiles near the wall could be measured. Freund[14] determined velocity, diffusivity, and viscosity profiles for the solvent. In that study, the solvent velocity approached zero at the wall, while the diffusivity decreased to a low but nonzero value. The viscosity increased to a large finite value in the 10 Å closest to the wall.

In order to overcome the limited spatial resolution of previous studies, I have conducted extensive NEMD simulations of electro-osmotic flow using a very simple model for the fluid and pore wall that still captures the essential physics. The model consists of counterions and monatomic nonpolar solvent molecules confined within a smooth cylindrical pore. Analogous NEMD simulations were also performed for the case of Poiseuille flow. This allowed the primitive fluid model to be validated by comparison with previous NEMD studies of Poiseuille flow and also enabled comparison of the Poiseuille flow and electro-osmotic flow behaviors.

II. METHOD

Nonequilibrium molecular dynamics simulation was used to directly observe electro-osmotic flow in small pores. The accuracy of this type of model is limited only by the force fields used to describe interactions between solvent molecules, counterions, and the pore walls, and the simulation size and duration, which are determined by computer resources and the computational efficiency of the simulation code. This general approach has recently been employed by several other groups.[10–14] Those studies all used detailed representations of the solvent and pore walls, and this limited the spatial resolution at which the velocity profile near the wall could be measured. One reason for this was that the computational cost of the detailed models limited the duration of the simulations. Since the velocity profiles are statistical averages over the entire simulation, shorter simulations result in higher statistical uncertainty which limits the achievable spatial resolution. A second reason was that the location of the solid surface could only be defined in an average sense. In other words, the fluid density did not become zero at a precise point, but decayed gradually to zero in an angstrom-thick region. While this effect is perfectly physical, it limits the resolution of features in the density and velocity profiles which depend on distance from the pore wall.

In order to provide a clear picture of what is happening close to the walls, I chose the simplest possible physical model that still captures the essential physics. Both solvent and counterion particles interacted with the Lennard-Jones 12-6 potential,

$$u(r_{ij}) = 4\epsilon_{ij}\left[\left(\frac{\sigma_{ij}}{r_{ij}}\right)^{12} - \left(\frac{\sigma_{ij}}{r_{ij}}\right)^{6}\right], \tag{1}$$

where r_{ij}, ϵ_{ij}, and σ_{ij} are the separation, Lennard-Jones well depth and Lennard-Jones diameter, respectively, for the pair of atoms i and j. The diameters for the solvent and counterion were chosen to approximately match the sizes of the water molecule and the sodium ion, following Goulding *et al.*[16] The masses were also taken to be those of water and the sodium ion. The diameter for the solvent-ion cross-interaction was chosen as the arithmetic mean of the self-interactions. The well depth was set to k_BT, where k_B is Boltzmann's constant and T is the temperature of the system, 300 K. Each counterion was assigned a charge of $q=+1e$ (e is the electronic charge), while the solvent particles were neutral. In order to approximately describe the polarity of real water, counterion–counterion electrostatic interactions were calculated using a screened Coulomb interaction,

$$u_e(r_{ij}) = \frac{q^2}{4\pi\epsilon_0\epsilon_r r_{ij}}, \tag{2}$$

where ϵ_0 is the dielectric permittivity of vacuum and ϵ_r is the relative permittivity of the fluid, which was set to 80. The numerical values of the force field parameters are listed in Table I.

TABLE I. Solvent and counterion force field parameters.

Species	ϵ (kcal/mol)	σ (Å)	q (e)	m (g/mol)
Solvent	0.5961	3.2	0	18.0
Counterion	0.5961	1.94	+1	23.0

In order to eliminate uncertainty about the location of the fluid boundary and maximize spatial resolution of the fluid velocity profile in the vicinity of the wall, the solid–fluid interaction was represented by a stochastic scattering boundary condition. The pore wall was treated as an impenetrable cylindrical wall of radius R_c, aligned with the x axis. Particles crossing the cylindrical surface located at $R_\alpha = R_c - \sigma_\alpha/2$ underwent diffuse inelastic scattering. This corresponded to instantaneous adsorption and desorption of the particles at a perfectly smooth wall located at $r=R_c$. The postcollisional velocity of the particle was generated from a Maxwellian distribution, as derived by MacElroy and Boyle,[17]

$$\xi_1 = (mv_0^2/2kT+1)e^{-mv_0^2/2kT}, \tag{3a}$$

$$v_r = -v_0\sqrt{\xi_2}, \tag{3b}$$

$$v_a = v_0\sqrt{1-\xi_2}\cos 2\pi\xi_3, \tag{3c}$$

$$v_c = v_0\sqrt{1-\xi_2}\sin 2\pi\xi_3, \tag{3d}$$

where v_0 is the postcollisional particle speed and v_r, v_a, and v_c are the radial, axial, and circumferential postcollisional velocity components. ξ_1, ξ_2, and ξ_3 are three independent uniform random numbers on (0,1). Equation (3a) was solved using Newton's method.

A check for collisions with the wall was performed at every time step during the particle position update. If the updated position lay outside the cylinder, the location of the collision event in space and time was estimated by assuming a constant particle velocity during the precollisional portion of the time step. The correct updated position of the particle

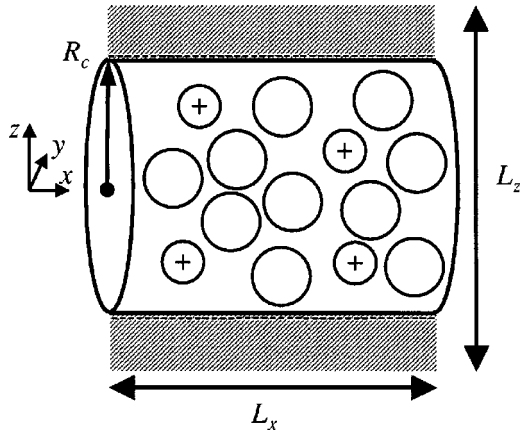

FIG. 1. Schematic diagram of the simulation box. The system consisted of positively charged counterions and neutral solvent particles confined by an impenetrable cylindrical negatively charged surface.

was obtained by advancing the particle from the collision location through the postcollisional portion of the time step with the postcollisional velocity.

This stochastic scattering boundary condition is similar to that used by Trozzi and Ciccotti[5] and has several advantages. It enables the exchange of thermal energy and momentum with the wall. It also provides a precise identification of the location of the fluid boundary (although this location is different for the solvent and counterion species). Specifically, the density of each species is a maximum at $r=R_\alpha$, and zero for $r>R_\alpha$. The main disadvantage is that the wall interaction is purely entropic, and so it is difficult to directly modify the adsorption affinity of each species.

The simulations reported here consisted of 1375 solvent particles and 31 counterions in a cylindrical pore of radius $R_c=20$ Å. The cylinder representing the pore wall was located at the center of a rectangular box, with its axis running parallel to the x direction, as illustrated schematically in Fig. 1. The x, y, and z dimensions were $L_x=39.52$ Å, $L_y=80.0$ Å, and $L_z=80.0$ Å, respectively. L_x was chosen so that the linear charge density carried by the counterions was equal and opposite to a surface charge density q_w of -0.1 C/m^2 on the cylindrical pore wall. Because the electric field inside an infinitely long charged cylinder is zero, q_w plays no role in the simulation, other than to indicate the number of counterions in the simulation. The number of solvent atoms was chosen so that the total mass density of the fluid was 1.0 g/cm^3.

Electrostatic interactions were calculated using PPPM Ewald summation, with a Gaussian decay constant of $G=0.288$ Å^{-1}. The real-space contribution to the Ewald sum, as well as all Lennard-Jones interactions, were truncated at 10.0 Å. The Lennard-Jones interaction was shifted to remove the small jump in energy at the truncation point. The reciprocal space contribution to the electrostatic energy was calculated using a $6\times15\times15$ mesh. The dimensions L_y and L_z were chosen to be sufficiently large so that the effect of electrostatic interactions between periodic images of the counterions was negligible. This was determined by comparing counterion density profiles obtained with successively larger values of L_y and L_z. This test was also used to choose values for other key simulation parameters, including the number of PPPM mesh points, the short-range cut-off distance and the box length in the x-direction. It should be noted that the simulation parameters were optimized for the particular calculations presented in this paper, but they may be unsuitable for other purposes. A considerably finer PPPM mesh would be required to resolve the electric field due to a multisite polar solvent. In addition, accurate measurement of the electrostatic energy would require either larger values of L_y and L_z or else a suitable correction for the effect of periodic images. The contribution of the wall charge to the electrostatic energy would also need to be included. These corrections make no contribution to the forces and so were not required in this study.

The temperature of the system was controlled using a Nosé–Hoover thermostat applied only in the y and z directions, using a coupling frequency of 0.01 fs^{-1}. Since the position-dependent average axial velocity should not be included in the definition of temperature and this was not calculated until after the simulation was completed, we calculated the temperature only in terms of the y and z velocity components. The combination of thermostatting and the stochastic boundary was sufficient to maintain isothermal conditions throughout the channel, except in those cases where the average axial velocity was comparable to or greater than the thermal speed of the particles, as discussed below. The equations of motion were integrated in time using the velocity Verlet scheme, with a time step of 5 fs. All simulations were performed using the LAMMPS (Refs. 18–20) molecular dynamics code using two nodes of the Cplant Ross cluster (466 MHz Compaq alpha ev6 chips connected by Myrinet).[21] The computational speed was approximately 20 time steps/second.

The solvent and counterion particles were initially placed in the simulation box in hexagonal sheets oriented perpendicular to the cylindrical axis. The system was then equilibrated by running equilibrium molecular dynamics for 50 000 time steps. Equilibrium properties of the system were obtained by running equilibrium molecular dynamics for a subsequent one million time steps.

In order to observe fluid flow in the pore, an external force F_x parallel to the cylinder axis was applied to some or all of the particles in the system. For Poiseuille flow, the force was applied to all the particles in the system. For electro-osmotic flow, the force was applied only to the counterions. In both cases, the nonequilibrium molecular dynamics (NEMD) simulation was run for 10 000 time steps to allow the flow in the cylinder to reach steady state. Following this, the NEMD simulation was run for six million time steps. The particle positions, velocities, and forces were saved after every one hundred time steps.

In the electro-osmotic flow simulations, the use of an applied field to drive the flow is consistent with the true physical situation. In response to a voltage differential imposed on the ends of a long capillary, the mobile charge in the capillary will quickly arrange itself to create a constant electric field between the two ends. This field then results in a spatially invariant axial force on all the charged particles in the system. In the Poiseuille flow simulations, consistency

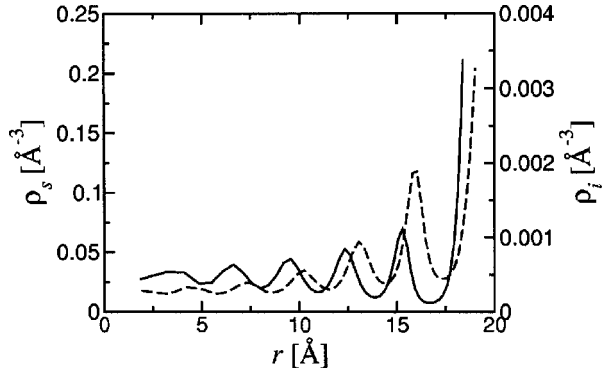

FIG. 2. Plot of solvent density (solid line, left axis) and counterion density (dashed line, right axis) as a function of distance from the center of the pore.

with the physical situation is not self-evident. Poiseuille flow occurs when a hydrostatic pressure differential is imposed on the ends of a long capillary. This then results in a spatially invariant axial pressure gradient. However, in the simulations, the pressure gradient which corresponds to the applied force on each particle is not constant. This point has been discussed in some detail by Todd *et al.* I follow their expedient in assuming that the Poiseuille flow simulations do indeed correctly represent the physical situation of Poiseuille flow.

III. RESULTS

A. Equilibrium properties

Figure 2 shows the solvent and counterion density as a function of radial position in the pore, obtained from the equilibrium simulation. Both the solvent and counterions have a layer of maximum density at the point of contact with the wall, R_α ($R_s = 18.4$ Å and $R_i = 19.03$ Å, respectively), with weak layering occurring in the second and subsequent layers. These profiles can be understood in terms of liquid theory and electrostatics.[22] The solvent concentrates at the wall because this provides the most efficient packing, which increases the overall translational entropy of the fluid. The subsequent weaker layers of solvent are spaced about one solvent diameter apart. Most of the counterions concentrate at the wall to minimize the electrostatic repulsion between counterions. Thermal excitation and solvation effects ensure that some of the counterions still reside away from the wall. These counterions tend to concentrate in a peak located about one solvent–ion diameter inside the nearest solvent layer, where the favorable contacts with solvent particles are maximized. This explains why the distance between the first and second counterion layers is greater than that between the second and third layers.

TABLE II. Average solvent and counterion axial velocities from Poiseuille flow simulations.

F_x (10^{12}) N/mol	u_s (m/s)	u_i (m/s)	μ (mPa s)
0.01	0.6(1)	0.5(4)	0.48(8)
0.10	6.1(2)	5.5(4)	0.45(2)
1.00	62.8(2)	57.4(4)	0.443(1)
10.00	966.0(4)	886.0(20)	0.2881(1)

TABLE III. Average solvent and counterion axial velocities from electro-osmotic flow simulations.

F_x (10^{12} N/mol)	E_x (10^7 V/m)	u_s (m/s)	u_i (m/s)	ζ (V)	D_i (10^{-9} m^2/s)
1.0	1.036	1.1(2)	2.7(4)	−0.15(3)	3.9(6)
5.0	5.182	6.0(2)	14.5(4)	−0.165(5)	4.2(1)
10.0	10.36	12.1(2)	29.4(4)	−0.165(3)	4.32(6)
20.0	20.73	24.3(2)	59.5(4)	−0.166(1)	4.39(3)
50.0	51.82	61.6(2)	158.9(4)	−0.168(1)	4.85(1)
100.0	103.6	128.0(2)	365.5(7)	−0.1737(3)	5.93(1)

B. Average transport properties

In performing nonequilibrium molecular dynamics simulations, it is important to use an appropriate value for the applied field strength. In both cases simulations were performed for a range of values. The results of these simulations are shown in numeric form in Tables II and III. The primary result from each simulation is the average axial solvent velocity u_s and the average axial counterion velocity u_i. These were obtained by averaging over all times and all particles of that species. Figure 3 shows u_s and u_i versus applied field strength, on a log–log scale. We can see that in all cases the velocity increases roughly linearly with the applied field strength. The statistical uncertainty is independent of the applied field strength, as it is controlled by the thermal speed of each species. Hence, the relative statistical uncertainty of the measured average velocities decreases linearly with the applied field strength.

For Poiseuille flow, the solvent and counterion velocities are identical within statistical uncertainty. The relationship of velocity to applied field strength can be examined more quantitatively by comparing with the well-known Hagen–Poiseuille formula for laminar flow in an cylindrical capillary,[23]

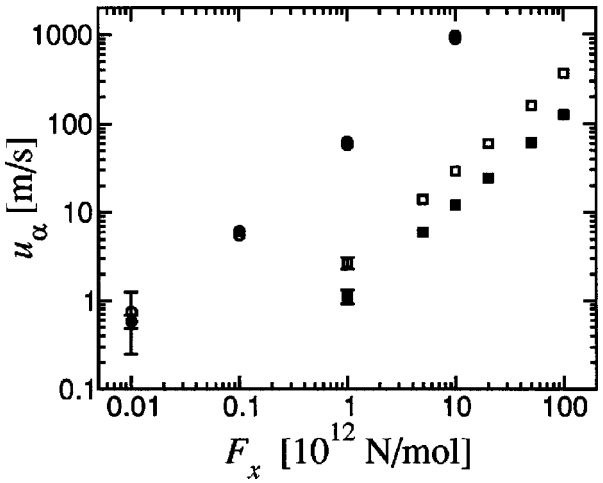

FIG. 3. Plot of solvent (open) and counterion (filled) average velocities vs applied field strength for Poiseuille (circle) and electro-osmotic (square) flow. Except where shown, error bars are smaller than symbols.

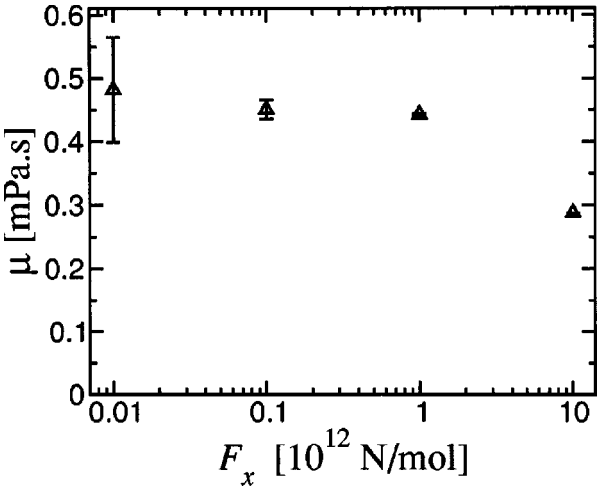

FIG. 4. Plot of viscosity as a function of applied field for Poiseuille flow.

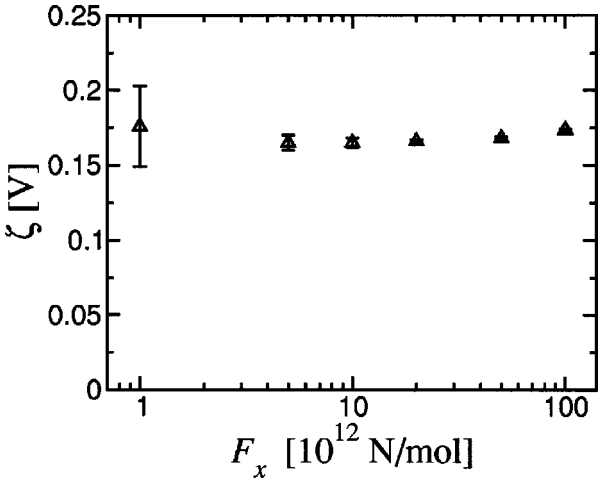

FIG. 5. Plot of ζ potential as a function of applied field for electro-osmotic flow.

$$u_s = -\frac{R_c^2}{8}\frac{\nabla P}{\mu}, \tag{4}$$

where ∇P is the pressure gradient along the capillary, assumed to be independent of position and μ is the shear viscosity of the fluid, also assumed to be independent of position. In order to obtain the effective pressure gradient for each simulation, the applied field strength was divided by the average molar volume of 18 cm^3/mol. Estimates of the fluid viscosity were then obtained from Eq. (4), and are shown in Fig. 4.

It should be noted that Eq. (4) assumes no slip at the fluid–wall boundary. In fact, the slip velocity at the wall was roughly 50% of the axial velocity at the center of the channel, so that Eq. (4) systematically underestimates the true viscosity of the fluid. This effect could be corrected for by subtracting the estimated slip velocity, which would result in proportionately larger values for the viscosities in all cases. In the following section the local shear stress and strain rate were used to calculate the local viscosity, which avoids the need to make assumptions about the boundary position and velocity.

At all but the highest applied field strength, the viscosity is independent of pressure gradient, with an average value of 0.45 ± 0.01 mPa s, which is typical for a dense atomic liquid. At the highest applied field strength, shear thinning is observed. The average flow velocity in this case is 966 m/s, whereas the thermal speed of the solvent is only 370 m/s. The next highest shear rate resulted in an average flow velocity of 62.8 m/s, which is well below the thermal speed, and the viscosity in this case appears to match that obtained at lower shear rates, within statistical uncertainty. Hence we find that NEMD simulations in which the average flow velocity is 10%–20% of the thermal speed provide the best tradeoff between accuracy and precision. Higher shear rates cause deviations from low-shear behavior, while using lower rates greatly reduces the statistical efficiency. A tenfold reduction in the applied field strength requires a 100-fold increase in the simulation length to achieve the same precision. The shear thinning that is observed when the streaming velocity is comparable to or greater than the thermal speed could have several possible causes including lack of energy conservation in the time integration scheme and a nonuniform temperature profile.

A similar analysis of the electro-osmotic NEMD simulations can be performed. Assuming that the electrical double layer is very small compared with the width of the channel, the electro-osmotic flow at a charged surface may be described by the Helmholtz–Smoluchowski equation,[1]

$$u_s = -\frac{\epsilon_0 \epsilon_r \zeta \nabla E}{\mu}, \tag{5}$$

where μ is the fluid viscosity, and $\nabla E = F_x/q$ is the electric field gradient parallel to the surface. ζ is the so-called ''zeta-potential'' which characterizes the sign and magnitude of the surface charge.

Assuming a nominal value of 1 mPa s for the fluid viscosity, values for the apparent ζ potential at each applied field strength were obtained from Eq. (5). These are plotted against the applied field strength in Fig. 5. Except for the highest field, the apparent ζ potential is independent of the applied field strength, with an average value of -0.167

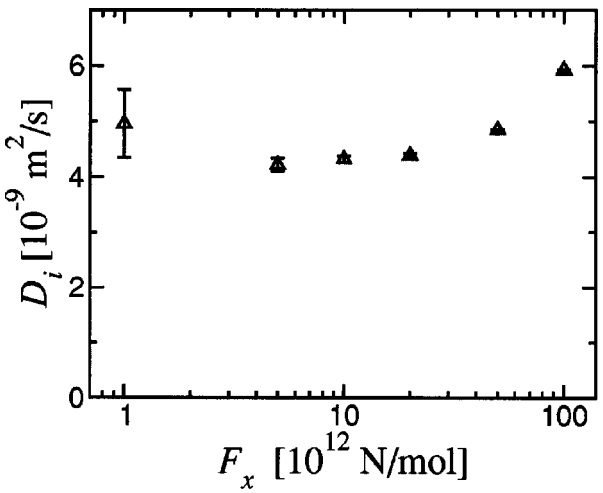

FIG. 6. Plot of ionic diffusion coefficient as a function of applied field for electro-osmotic flow.

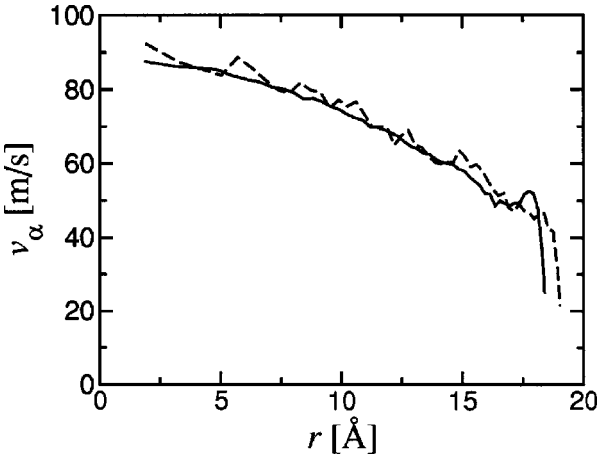

FIG. 7. Plot of solvent (solid) and counterion (dashed) velocity as a function of distance from center of pore for Poiseuille flow at an applied field strength of 10^{12} N/mol.

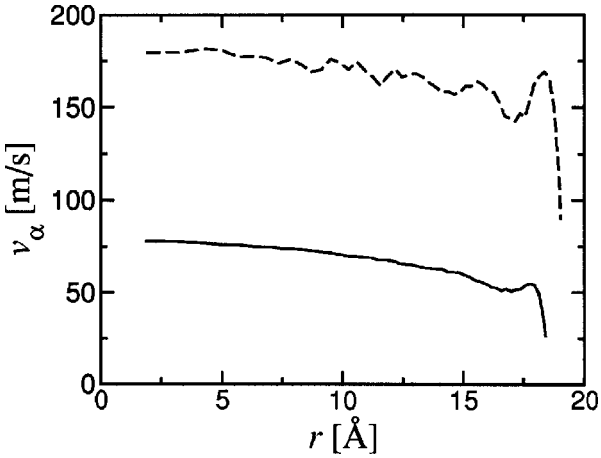

FIG. 8. Plot of solvent (solid) and counterion (dashed) velocity as a function of distance from center of pore for electro-osmotic flow at an applied field strength of 50×10^{12} N/mol.

±0.001 V. The ζ potential for silica glass under typical conditions is -0.1 V. The apparent ζ potential at the highest applied field strength was higher than the low field value. This is consistent with the shear thinning that was observed with Poiseuille flow. As for pressure driven flow, the transition from linear to nonlinear behavior occurs when the flow velocity approaches the thermal velocity of the fluid.

Finally, the difference between the counterion and solvent velocities can be used to estimate the ionic diffusion coefficient D_i, which is defined by the following constitutive relation:

$$u_i - u_s = -\frac{D_i}{k_B T} q \nabla E, \tag{6}$$

where q is the counterion charge. The ionic diffusion coefficient for each applied field strength was calculated from Eq. (6). The results are given in Table III and Fig. 6. The diffusion coefficient is independent of applied field strength at small field. However, compared to the ζ potential, nonlinear deviations occur at lower applied field strength, and deviations are more pronounced. This is perhaps due to the fact that the counterion velocity is more than twice that of the solvent and so approaches the thermal velocity at lower applied field strengths.

C. Local transport properties

In the previous section average transport properties were presented, obtained by averaging the species velocities over the entire channel cross section. In this section local transport properties will be presented, obtained by measuring species velocities as a function of radial position in the pore. The analysis was performed for all the applied field strengths that were simulated, but only results for the Poiseuille flow simulation with applied field strength 10^{12} N/mol and the electro-osmotic flow simulation with applied field strength 50×10^{12} N/mol are presented. As explained in the previous section, these applied field strengths provide an accurate description of the linear response of the fluid while minimizing the statistical error.

In order to sample the local fluid velocity, the cylindrical volume of radius R_α accessible to particles of each species was divided into 50 annular regions of equal volume. The average square distance from the center axis for these regions was then taken to be $(1-\frac{1}{2})(R_\alpha^2/50)$, $(2-\frac{1}{2})\times(R_\alpha^2/50),\ldots,(50-\frac{1}{2})(R_\alpha^2/50)$. In order to measure the slip velocity of particles very close to the wall, one additional annular region was included, twenty times smaller than the volume of the other regions, for which the average square particle position was $(2000-\frac{1}{2})(R_\alpha^2/2000)$. All the configurations saved during a simulation were used to compute the average axial velocity of the particles located in a given region. In this way, the velocity profile for each species was obtained.

Figure 7 shows the velocity profiles obtained from a Poiseuille flow simulation with an applied field strength of 10^{12} N/mol. The counterion velocity closely matches that of the solvent, but exhibits greater statistical uncertainty, due to the far smaller number of particles. In the center of the channel, the solvent velocity profile has the parabolic form predicted by continuum fluid mechanics. However, near the channel wall, several features occur that are beyond the reach of continuum theory. There is a nonzero slip velocity at the wall. In a region less than 1 Å thick the velocity increases rapidly to roughly twice the slip value.

The rapid doubling of the velocity can be understood by considering the infinitesimally thin region adjacent to the wall. The particles can be divided into two populations: postcollisional particles moving away from the wall and precollisional particles moving towards the wall. Because the particles undergo perfect diffuse scattering at the wall, the former population have an average axial velocity of zero, while the latter have a nonzero average velocity which I will define as v_{slip}. Since the net flux into the wall is zero, the two populations must be equal in size, and so the average axial velocity at the wall is $v_{\text{wall}}=v_{\text{slip}}/2$. The correlation between radial and axial velocity will decay rapidly with distance from the wall and should become small at a distance roughly equal to the mean free path of the fluid. In dense fluids, the mean free path is a small fraction of one particle

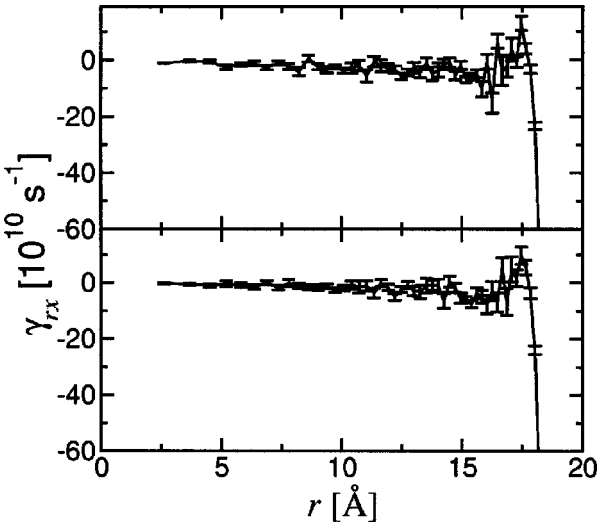

FIG. 9. Plot of solvent shear strain rate as a function of position for Poiseuille flow (top) and electro-osmotic flow (bottom). The data were obtained at applied field strengths of 10^{12} N/mol and 50×10^{12} N/mol, respectively.

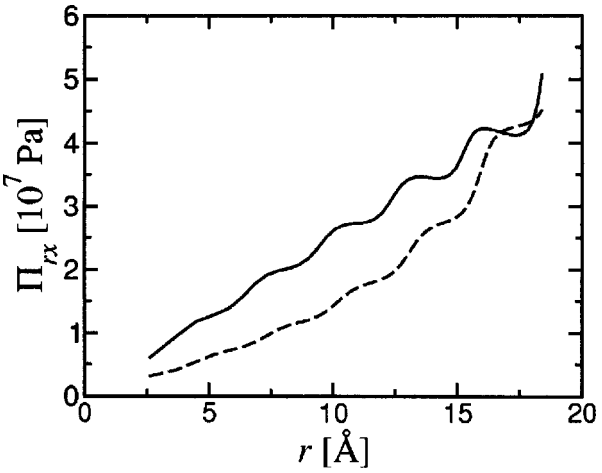

FIG. 10. Plot of shear stress as a function of position for Poiseuille flow (solid) and electro-osmotic flow (dashed). The data were obtained at applied field strengths of 10^{12} N/mol and 50×10^{12} N/mol, respectively.

diameter, or a fraction of one angstrom. Hence the average axial velocity in the very thin region near the wall v_{wall} provides an accurate measure of the full slip velocity, which is twice the wall value.

Just beyond the point where the full slip velocity is achieved, the velocity profile exhibits a pronounced maximum, followed by a minimum. It then becomes smoothly parabolic. This nonmonotonic velocity profile close to the wall has previously been observed by Travis *et al.* for Poiseuille flow in a slit pore.[8,9] This behavior is discussed further below.

Figure 8 shows the velocity profiles obtained from an electro-osmotic flow simulation with an applied field strength of 50×10^{12} N/mol. In this case, the counterion velocity is considerably higher than that of the solvent. Away from the wall, the velocity profiles are almost flat. The small residual slope is due to the nonzero density of counterions extending into the center of the pore. Again we see a nonzero slip velocity at the wall that is roughly half of the full slip velocity. Both the solvent and counterion profiles exhibit a pronounced maximum and minimum.

In order to compare the velocity profiles with continuum theory, finite differences were used to calculate the derivative of the solvent velocity profiles with respect to r, which corresponds to the shear rate $\gamma_{rx}(r)$. The counterion velocity was not included in the analysis. Because the counterion velocity is always greater than the solvent velocity, it introduces a spurious oscillatory contribution to the shear rate, proportional to the derivative of the counterion/solvent density ratio. Figure 9 shows the shear rate profile in the fluid under Poiseuille and electro-osmotic flow. Each simulation was divided into 20 blocks of 150 000 time steps and the variance over blocks was calculated for each data point. The error bars represent the expected standard deviation of the average over the blocks. The two cases appear very similar. Far from the wall the shear rate is negative, with magnitude increasing linearly with r, consistent with continuum fluid mechanics. As the wall is approached, the shear rate passes through a minimum, becomes positive, passes through a maximum and then approaches a large negative value at contact with the wall. At lower applied field strengths, the shear rates are proportionately small and so the data is noisier, but the same behavior can be observed.

A simple force balance on the cylindrical region of radius r allows us to write the following expression for the average shear stress at point r in the fluid:

$$\Pi_{rx}(r)=\frac{1}{r}\int_0^r \sum F_i\rho_i(r')r'dr', \tag{7}$$

where $\Pi_{rx}(r)$ is the shear stress acting in the axial direction across the cylindrical surface of radius r. F_α is the applied field acting on particles of species α and $\rho_\alpha(r)$ is the local density of species α at r. In our case, the summation only has

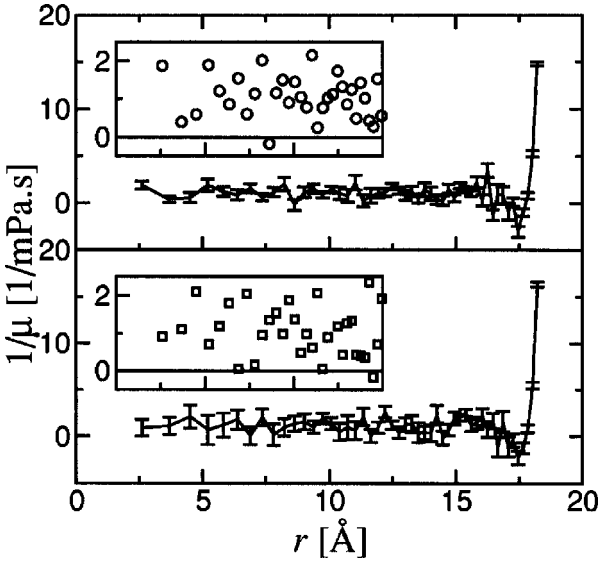

FIG. 11. Plot of reciprocal viscosity as a function of position for Poiseuille flow (top) and electro-osmotic flow (bottom). The data were obtained at applied field strengths of 10^{12} N/mol and 50×10^{12} N/mol, respectively. The inset figures show the data points sampled on the range 0–15 Å, plotted on an expanded scale.

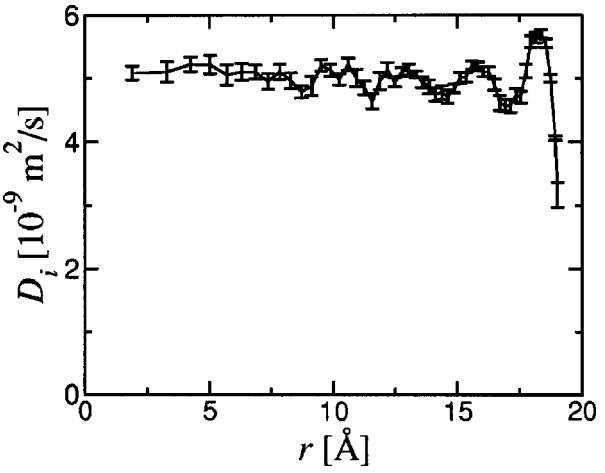

FIG. 12. Plot of ionic diffusion coefficient as a function of position for electro-osmotic flow at an applied field strength of 50×10^{12} N/mol.

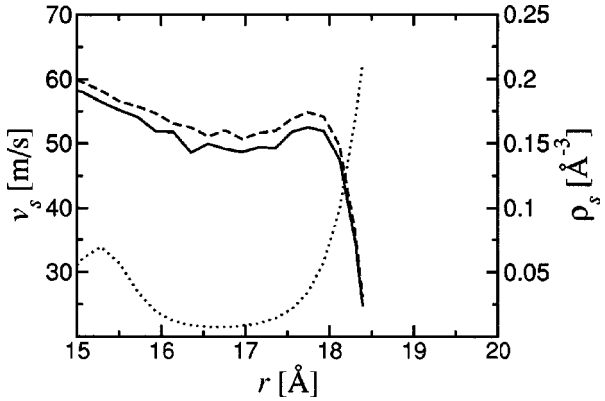

FIG. 13. Overlay of solvent velocity profiles (left axis) and solvent density profile (right axis) for the region close to the pore wall. The solid line is for pressure driven flow with an applied field strength of 10^{12} N/mol and the dashed line is for electro-osmotic flow with an applied field strength of 50×10^{12} N/mol. The density profile is given by the dotted line.

two terms, the solvent and the counterions. The densities are obtained from the profiles shown in Fig. 2. In the case of Poiseuille flow in a slit pore, this type of mean-field expression for the shear stress was found to agree well with the average of the instantaneous stress calculated directly from interparticle forces, while providing much better statistical precision.[24] The resultant shear stress profiles for the two cases are shown in Fig. 10. The statistical uncertainty in the data is smaller than the linewidths. The Poiseuille shear stress is essentially linear in r, with some superimposed weak oscillations due to ordering of the fluid near the wall. The electro-osmotic shear stress increases nonlinearly with r, as the charge density is higher near the wall.

A local viscosity $\mu(r)$ can now be defined in terms of the local shear rate $\gamma_{rx}(r)$ and the local shear stress $\Pi_{rx}(r)$ by invoking the linear constitutive relation for momentum transport in simple fluids, also known as Newton's law,

$$\Pi_{rx}(r) = -\mu(r)\gamma_{rx}(r). \tag{8}$$

Figure 11 shows the reciprocal of $\mu(r)$ as a function of position for Poiseuille and electro-osmotic flow. The two results are remarkably similar. In both cases, the viscosity is constant in the region $r<15$ Å (Fig. 11 insets). This indicates that beyond two monolayers from the wall, both Poiseuille and electro-osmotic flow are well described by continuum mechanics. Averaging over all the data points in this region yielded an average viscosity of 0.92 ± 0.01 mPa s for Poiseuille flow and value of 0.90 ± 0.02 mPa s for electro-osmotic flow. The fact that these independent simulations of two different transport processes result in statistically equivalent values for the viscosity validates the simulation methodology and analysis.

The microscopic viscosity is higher than the macroscopic values reported in Table II. This is due to the fact that the macroscopic calculation included the effect of wall slip, which tends to lower the apparent viscosity.

Since the ζ potential characterizes the fluid–solid interface, it is not meaningful to define a local ζ potential. It is meaningful to define a local ionic diffusion coefficient. To do this, the average axial species velocities in Eq. (6) were replaced by the local values. The resultant plot of $D_i(r)$ is shown in Fig. 12. The diffusion coefficient is constant in the region $r<15$ Å, with an average value of $4.99\pm0.02\times10^{-9}$ m^2/s. This is very close to the macroscopic value reported in Table III, despite the fact that the microscopic diffusion coefficient varies strongly in the region near the wall. The net effect of these variations is almost zero.

IV. DISCUSSION

A detailed analysis of the velocity profiles obtained from simulations of both Poiseuille and electro-osmotic flow through a nanopore showed that the continuum description of these flow phenomena is accurate except in the region very close to the pore wall, where the continuum assumption breaks down. At a distance of more than two monolayers from the wall, the local viscosity becomes constant. Moreover, close agreement was found between the values of the average viscosity in this region obtained from the Poiseuille flow simulation and the electro-osmotic flow simulation.

However, in the first two monolayers, noncontinuum behavior was observed. This was manifested by regions of negative and divergent viscosity for both Poiseuille flow and

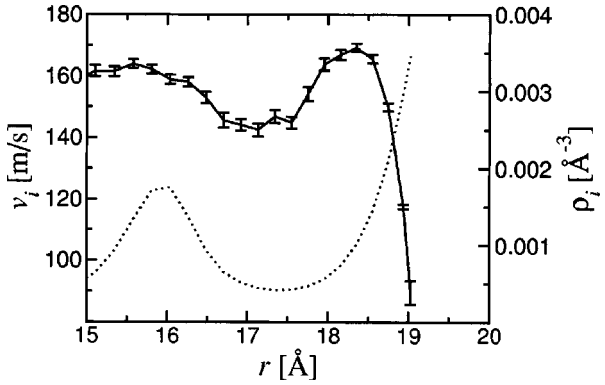

FIG. 14. Overlay of counterion velocity profile (solid line, left axis) and counterion density profile (dotted line, right axis) for the region close to the pore wall. The velocity profile is for electro-osmotic flow at an applied field strength of 50×10^{12} N/mol.

electro-osmotic flow. The extremely anomalous nature of the viscosity close to the wall is not an artifact of the stochastic scattering boundary that we chose to represent the pore wall. Qualitatively similar viscosity profiles have been observed in several previous NEMD studies, all of which represented the pore wall using a freely vibrating lattice of atoms.[8,9,25]

Efforts to resolve the apparent anomalous viscosities with continuum theory have lead to several proposed modifications to Newtonian rheology, including nonlocal generalizations[25] and a wave vector dependent viscosity.[9] However, since the anomalous behavior is obviously due to the underlying atomistic structure of the fluid near the wall, one should not expect continuum concepts such as viscosity to apply. Instead, it is helpful to examine the velocity data directly.

Figure 13 shows the solvent velocity profiles from the Poiseuille and electro-osmotic flow simulations, expanded in the region near the wall. Overlaid on this is the solvent density profile. Even without correcting for the different stress profiles, the velocity profiles from the two simulations agree very closely. In both cases the velocity rises rapidly with increasing distance from the wall, passing through a sharp maximum, followed by a more extended trough of low velocity. Beyond this trough, the velocity increases smoothly. The peak in the velocity occurs at the edge of the first monolayer or about 0.6 Å from the solvent–wall contact point. The trough covers the entire region of depleted density that lies between the first and second monolayers.

Figure 14 shows the counterion velocity profile from the electro-osmotic flow simulation, expanded in the region near the wall. Overlaid on this is the counterion density profile. The counterion velocity profile is similar to that of the solvent. The counterion velocity peak occurs at the edge of the first counterion monolayer and is about 0.6 Å from the counterion–wall contact point.

This suggests that the variations in velocity are due to the underlying structure of the fluid at the wall. More specifically, the peaks in the solvent and counterion velocities appear to occur near the outer edge of the first monolayer and at a fixed distance from the point of contact with the wall. It makes sense that particles in this region move faster than particles closer to the wall, where the interaction with the wall is stronger. It is less obvious why these particles also move faster than particles farther away from the wall. Two possible causes are the two-dimensional ordering of the fluid and variations in force density.

The two-dimensional ordering of the fluid in the first monolayer may enhance cooperative motion between particles, resulting in a higher average velocity compared to the more disordered fluid farther from the wall. The applied force density increases in proportion to the density of solvent or counterions, and particles experiencing a higher force density will be less susceptible to retardation by collisions with slower particles that have just collided with the wall. This might cause particles in the low density region between the first and second monolayers to move more slowly than particles at the edge of the first monolayer. Opposing this hypothesis is the fact that the location of the solvent velocity peak is identical in both Poiseuille and electro-osmotic flow, even though the force density profiles are quite different.

The simulations presented here have served to confirm the existence of enhanced transport rates in the first layer of fluid, both in Poiseuille and electro-osmotic flow. They also demonstrate that the effect is a generic property of confined fluids, i.e., it occurs for both structureless and atomistic representations of the pore wall. Comparison of density profiles and velocity profiles suggest that the enhanced transport is caused by the strongly two-dimensional ordering of the fluid at the wall, but this has not been conclusively demonstrated. One possible way to do so would be to measure velocity correlations between neighboring particles as a function of distance from the wall.

Note added in proof: After completion of the manuscript I became aware of an NEMD study of electro-osmotic flow by Qiao and Aluru.[26] Their model and results were similar to those of Freund.[14] They also developed a convenient methodology for using the velocity profile near the wall obtained from an NEMD simulation to provide a velocity boundary condition for continuum simulations of electro-osmotic flow.

ACKNOWLEDGMENTS

I am grateful to John Aidun for useful discussions on the limitations of continuum theories. Sandia is a multiprogram laboratory operated by Sandia Corporation, a Lockheed Martin company, for the United States Department of Energy under Contract No. DE-AC04-94AL-85000.

[1] R. F. Probstein, *Physicochemical Hydrodynamics*, 2nd ed. (Wiley–Interscience, New York, 1994).
[2] C. L. Rice and R. Whitehead, J. Phys. Chem. **69**, 4017 (1965).
[3] R. J. Gross and J. F. Osterle, J. Chem. Phys. **49**, 228 (1968).
[4] Y. Yang and P. Pintauro, AIChE J. **46**, 1177 (2000).
[5] C. Trozzi and G. Ciccotti, Phys. Rev. A **29**, 916 (1984).
[6] J. Koplik, J. R. Banavar, and J. F. Willemsen, Phys. Fluids A **1**, 781 (1989).
[7] P. A. Thompson and M. O. Robbins, Phys. Rev. A **41**, 6830 (1990).
[8] K. P. Travis, B. D. Todd, and D. J. Evans, Phys. Rev. E **55**, 4288 (1997).
[9] K. P. Travis and K. E. Gubbins, J. Chem. Phys. **112**, 1984 (2000).
[10] J. Lyklema, S. Rovillard, and J. DeConinck, Langmuir **14**, 5659 (1998).
[11] T. Mattke and H. Kecke, J. Colloid Interface Sci. **208**, 555 (1998).
[12] T. Mattke and H. Kecke, J. Colloid Interface Sci. **208**, 562 (1998).
[13] X. Din and E. Michaelides, AIChE J. **44**, 35 (1998).
[14] J. Freund, J. Chem. Phys. **116**, 2194 (2002).
[15] S. T. Cui and H. D. Cochran, J. Chem. Phys. **117**, 5850 (2002).
[16] D. Goulding, J. Hansen, and S. Melchionna, Phys. Rev. Lett. **85**, 1132 (2000).
[17] J. MacElroy and M. Boyle, Chem. Eng. J. **74**, 85 (1999).
[18] URL http://www.cs.sandia.gov/~sjplimp/lammps.html
[19] S. Plimpton, J. Comput. Phys. **117**, 1 (1995).
[20] S. J. Plimpton, R. Pollock, and M. J. Stevens, in Proceedings of the Eighth SIAM Conference on Parallel Processing for Scientific Computing, Minneapolis, MN, 1997.
[21] R. Brightwell, L. A. Fisk, D. S. Greenberg, T. Hudson, M. Levenhagen, A. B. Maccabe, and R. Riesen, Parallel Comput. **26**, 243 (2000).
[22] J.-P. Hansen and I. R. McDonald, *Theory of Simple Liquids*, 2nd ed. (Academic, London, 1986).
[23] B. Massey, *Mechanics of Fluids*, 4th ed. (Van Nostrand Reinhold, London, 1979).
[24] B. D. Todd, D. J. Evans, and P. J. Daivis, Phys. Rev. E **52**, 1627 (1995).
[25] L. A. Pozhar, Phys. Rev. E **61**, 1432 (2000).
[26] R. Qiao and N. R. Aluru, J. Chem. Phys. **118**, 4692 (2003).